Electron Beam Properties for Touchless Potential Sensing of Complex Geometry Spacecraft

Kaylee Champion* and Hanspeter Schaub †

Department of Aerospace Engineering Sciences, University of Colorado Boulder, CO, United States.

In hazardous charging environments, spacecraft components may charge to highly different potentials and experience dangerous arc discharges during docking operations. To avoid dangerous arc charges, a servicer spacecraft may touchlessly determine the potential of the target spacecraft, or the spacecraft it is docking with. Novel active potential sensing techniques are under investigation to determine the potential of a nearby spacecraft in Geosynchronous and cislunar space. These methods utilize an electron beam to excite secondary electron and x-ray emissions that may then be measured to determine the potential of a target with respect to oneself. Inhomogeneous electric fields due to complex spacecraft geometries make secondary electron trajectories difficult to predict and limit the regions in which electron emissions may be detected. Therefore, properties of the electron beam, including energy, half angle, and angle of deflection are altered such that secondary electrons are excited and may be detected by a servicer approaching a target.

I. Introduction

Novel active sensing methods are under consideration to touchlessly sense the electrostatic potential of non-cooperative objects in Geosynchronous Equatorial Orbit (GEO) and cislunar space. Such approaches make use of a positively charged servicing craft that directs an electron beam or ultraviolet (UV) laser at the object of interest so that low-energy secondary electrons [1, 2], x-rays [3, 4], and photoelectrons [5] may be emitted from its surface (Fig. 1). The servicer measures the incoming signals and, knowing its own potential, infers that of the target. This information can be employed to compensate for electrostatic perturbations in close-proximity multi-spacecraft operations [6, 7], minimize the risk of electrostatic discharge during rendezvous, control spacecraft formations [8], and detumble [9] or reorbit [10–14] space debris by means of electrostatic forces, among others.

The electric field produced by charged spacecraft with complex geometry is highly inhomogeneous, resulting in complex electron trajectories. Previous work has been conducted to characterize the secondary electron trajectories and relative positions where secondaries are detectable for various spacecraft potentials and shapes [15–18]. Typically, electron emission are only detectable for approximately 10% of servicer positions with respect to the target when the electron beam parameters are held constant [15, 19]. However, the percent of positions in which secondaries can be detected may be increased by manipulating electron beam parameters. Essentially, the beam parameters are altered such that source regions, or regions on a target in which emissions reach the servicer, are found. X-ray emissions have been found to be detectable for approximately 70% of relative servicer positions [18]. Therefore, the beam parameters may again be manipulated to increase the percent of relative positions in which x-rays are detected.

The goal of this work is to develop a control that manipulates a servicer's electron beam parameters, including energy and deflection angles, such that detectable secondary electron and x-ray emissions are excited from a target. The problem scenario is given in Section II, an overview of the touchless potential sensing concepts and measurement methods is given in Section III, and the models used in this work are described in Section IV. The characterization of beam parameters, their impact on detected emissions, and developed beam controls that alter these beam properties are presented in Section V. The beam controls are tested in the context of an optimized docking problem in VI, and conclusions and future work are presented in VII.

*NSTGRO Fellow, Graduate Research Assistant, Department of Aerospace Engineering Sciences, University of Colorado Boulder, CO, United States. AIAA student member.email:kach7227@colorado.edu

†Professor and Department Chair, Schaden Leadership Chair, Glenn L. Murphy Chair in Engineering, Ann and H.J. Smead Aerospace Engineering Sciences, AIAA and AAS Fellow.

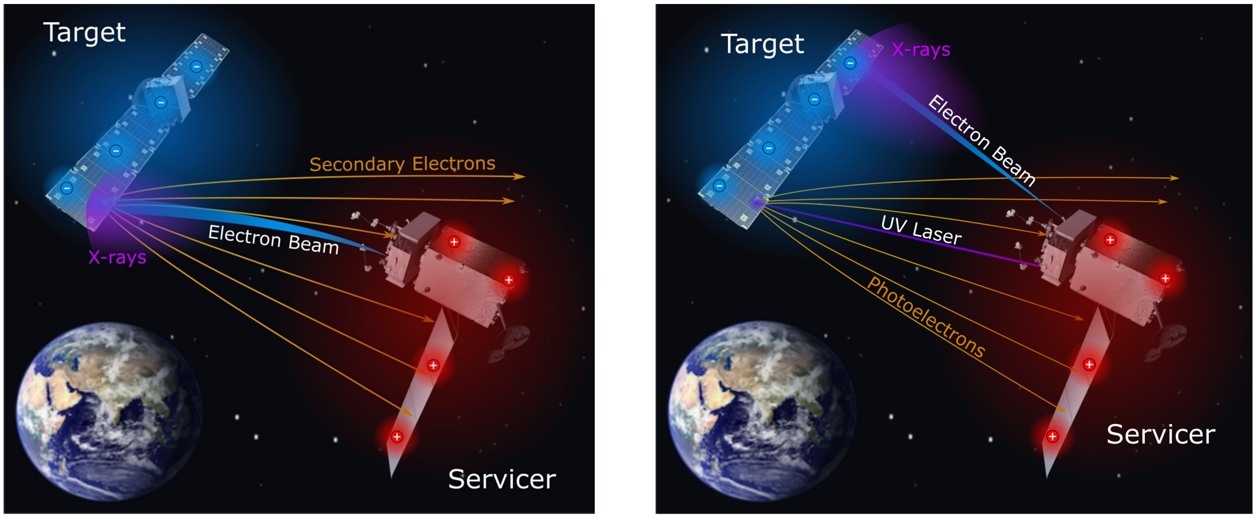

Fig. 1 Conceptual representation of the secondary electron generation (left) and combined photoelectron and x-ray generation processes (right).

II. Problem Scenario

High altitude earth orbits (HEO) and cislunar regions, such as the plasmasheet, are considered hazardous charging environments, as shown in Fig. 2. The magnitude of potential on a spacecraft is highly dependent on the geometry, material, and sunlit area [20, 21]. Therefore, even if two spacecraft are in the same environment, it is possible for them to achieve significantly different potentials. This is particularly dangerous during docking operations, as damaging arc discharges may occur between two spacecraft with different potential. Furthermore, uncertainties in spacecraft and plasma properties reduce the accuracy of spacecraft charging computational tools, such as NASCAP-2k and SPIS, and an in-situ method of detecting neighboring spacecraft potentials is necessary for an accurate assessment during proximity operations [22].

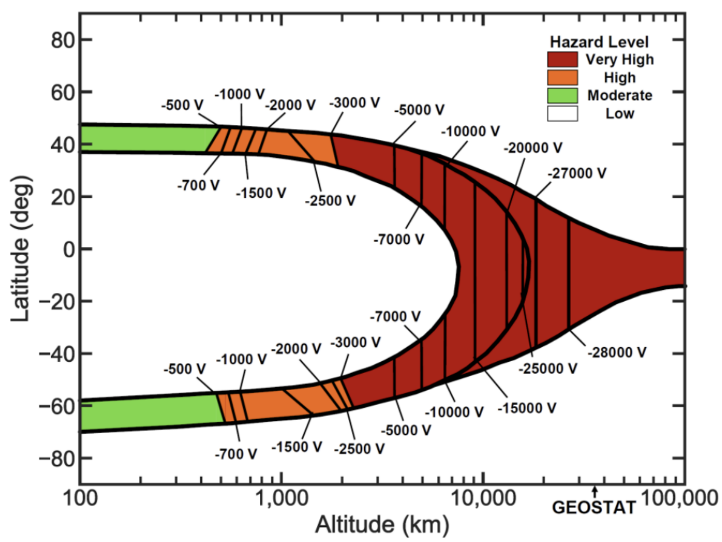

Fig. 2 Earth regimes of concern for charging hazards based on data from DMSP and Freja. The worst spacecraft potentials are shown [23].

In addition to being subject to arc discharges, charged spacecraft may exert upwards of 5 mN · m of torque during extreme charging events in high earth orbit conditions [7]. As a result, it is desirable to minimize the electrostatic torques between high potential spacecraft during proximity operations. Previously, an optimized guidance control was created in [7] such that the final rotation rate of a charged target is minimized as a charged servicer docks with it. The control involves the servicer approaching the target at a constant velocity with ten minute holds at 20, 10, and 3 meters for guidance verification, and it is assumed it is possible to determine the target potential at all desired points. The validity of this assumption is investigated, and the electron beam control is implemented at the pre-designed holds.

III. Touchless Potential Sensing Overview

Detailed descriptions of secondary electron [2, 16, 24] and x-ray emissions [3, 18] and the related particle tracing simulation [5] is presented in previous works. A brief overview of these emissions and sensing techniques is provided for context

A. Sensing Secondary Electron Emissions

Incoming electrons with an energy greater than the work function of the surface material may generate secondary electrons. The secondary electron yield δ determines the probability of emission of secondaries per impacting electron. This value depends on the incidence energy E of the impinging electron and can be roughly approximated by the Sanders and Inouye yield model

$$\delta(E, 0) = c\left[e^{-E/a} - e^{-E/b}\right], \tag{1}$$

where $a = 4.3E_{\text{max}}$, $b = 0.367E_{\text{max}}$, and $c = 1.37\delta_{\text{max}}$ [25]. The parameters δ_{max} and E_{max} define the maximum yield and energy at the maximum. For this problem, aluminum is assumed for the spacecraft surfaces, with a yield δ_{max} of 0.97 and energy at maximum E_{max} yield of 300 eV. In other words, the closer the electron beam landing energy is to 300 eV, the higher the secondary electron yield. Once emitted, the energy of the secondary electrons is on the order of a few eV and follows a characteristic distribution with a peak at one third the work function of the material [26]. The angular distribution of the emissions follows Lambert's cosine law and is nearly independent of the angle of the incident electron [27].

The energies of the secondary electron emissions are determined using a Retarding Potential Analyzer (RPA). This instrument is a type of electrostatic analyzer (ESA) that is used to determine the energy distribution of ambient particles. To do so, a grid within the RPA is electronically biased such that only electrons with energy greater than the potential of the grid can enter and be measured. The grid potential is then increased, and the current is again measured. After "sweeping" through a range of potentials, a discrete distribution of the particle energies is obtained [28]. The speed at which this sweep occurs depends on the quality of the instrument's power supplies, and an individual measurement by an RPA may take from fractions of a second to a couple seconds. For example, The RPA on Parker Solar Probe, or the Solar Probe Cup, takes a 0.0034 to 0.2185 seconds per measurement [29], a compact RPA on a cubesat takes approximately 0.2 seconds per measurement [30], and the RPA used in in-house vacuum experiments at the University of Colorado Boulder takes a minimum of 2 seconds per measurement [31]. A speed of 1 second per measurement is assumed for this work. The RPA is set to sweep from 0 Volts to $E_B - E_S$, as the magnitude of the target potential must be lower than this in order for the beam to reach the target. Thus, a complete sweep may take from a few seconds to approximately a minute. Furthermore, the resolution is dependent on the instrument design, and uncertainty may vary from a fraction of a percent to several percent [29, 32]. A resolution of 2% is assumed for this problem, based on the RPA used in previous in-house experiments [18].

B. Sensing X-ray Emissions

X-ray emissions for touchless potential sensing utilizes bremsstrahlung and characteristic emitted from thick targets [33]. Bremsstrahlung x-rays are emitted in a spectrum, and approximations of this spectrum are available [3, 18]. It is also possible to define the x-ray emission yield, or the number of photons per second emitted by impacting electron, using the formula [34]

$$\epsilon(E, Z) = a\left(ZE + 16.3Z^2\right), \tag{2}$$

where $a \approx 1.2 \cdot 10^{-9}$ is an empirical constant, E is the energy of the incident electron, and Z is the material's atomic number. Aluminum is assumed as the surface material of the target, with an atomic number of 13. The characteristic electron yield is similarly approximated as [35, 36]

$$\sigma = N\left(\frac{E}{E_k} - 1\right)^a, \tag{3}$$

Fig. 3 Initial position of servicer (red) and target (blue) in SIMION.

where N = 1.5E-5, a = 1.63, and the characteristic emission energy E_k = 1.49 keV for aluminum.

The direction of the radiation emission is dependent on the incident angle of the electrons, and can be estimated as [34]

$$Q(\theta) = \frac{sin(\theta)^2}{(1-\beta cos(\theta))^5}, \tag{4}$$

where θ is the incident angle of the electron, and $\beta = v/c$ is the ratio of the electron velocity to the speed of light. However, previous experiments have shown that this overestimates the directional dependence, and measurements of target potential using x-rays are possible for scenarios in which the electron beam impacts a surface not facing away from the sensor with little change in uncertainty [4, 7].

X-ray emissions are measured using an x-ray spectrometer. Previous experiments utilize an Amptek X123 spectrometer with a 6 mm^2 collecting area and flight heritage Mini-XSS solar observatory mission [31]. The sensor has a resolution of approximately 120 Volts, and 1000 photons have been found to be sufficient to determine a target's potential [7].

IV. Modeling Approach

The system is composed of a servicer, based on SSL-1300, equipped with an electron beam and a target modeled after the GOES-R spacecraft. The SSL-1300 spacecraft is symmetric with a rectangular main body and two solar panels. The GOES-R spacecraft is asymmetric, with one solar panel and a boom. The spacecraft are assumed to be fully conducting. SIMION is employed to determine the beam and emission trajectories for these spacecraft, initial positions shown in Fig. 3. SIMION is a charged particle tracing software that determine the electric fields and particle trajectories based on the defined potential arrays.

A. Electrostatic Framework

SIMION computes the trajectory of each charged particle from Newton's second law

$$\frac{\mathrm{d}\mathbf{v}}{\mathrm{d}t} = \frac{q}{m}\mathbf{E}, \tag{5}$$

where $\mathbf{v}$, q, and m are respectively the particle velocity, charge, and mass, $\mathbf{E}$ is the electric field, and t is the time. Relativistic corrections are implemented when Lorentz's factor $\gamma = \sqrt{1 - v^2/c^2}$ exceeds 10^{-10}, with c being the speed of light. The electric field is derived from the electrostatic potential field V as

$$\mathbf{E} = \nabla V, \tag{6}$$

while V is computed by solving Laplace's equation

$$\nabla^2 V = 0 \tag{7}$$

in the simulation domain. SIMION employs a regular Cartesian mesh with boundary conditions determined by set potentials of each electrode (Dirichlet) or by the zero-derivative of the potential V (Neumann). The potentials of the electrodes can be individually adjusted in SIMION, and the additive property of the Laplace equation is utilized to determine the potential field, which is saved as a potential array. The development of the large scale SIMION model employed in this work is outlined in [37]. The potential array around the spacecraft has 40 cm element sizes. A more refined mesh of 20 cm results in an order of magnitude longer computational time, with negligible changes in particle trajectories.

B. Particle Emissions

The touchless electrostatic potential sensing and emissions model is built in SIMION by means of LUA user-defined functions. The secondary electron and photoelectron emission models have previously been developed in SIMION and are outlined in [2, 38]. In this model, the emissions are considered to be sensed if they impact the side of the main body of the servicer closest to the target, resulting in a collection area of 6.25 m^2.

X-ray emissions are implemented in the full-scale SIMION model for the development of the electron beam control for sensing x-rays. The photons are modeled as particles with zero charge such that they are not impacted by the electrostatic environment and follow rectilinear paths. The yield models described in Section III are utilized to determine the emitted photons per second emitted per incoming electron. The angular distribution of the emitted photons are defined to be isotropically emitted, as measurements using x-ray emissions have been found to be possible with small changes in uncertainty for all cases in which the electron beam does not impact a target a face directed opposite to the sensor [18].

C. Environmental Considerations

When a charged object, such as a spacecraft, is located in a plasma, the surrounding charged particles attempt to reorganize and shield the electric field of the particle. The measure of this phenomenon, or the measure of how far a charge's electrostatic effect persists, is known as the Debye length [39]. The electron Debye length is found using

$$\lambda_D = \sqrt{\frac{\epsilon_0 k_B T_e}{n_e q_e^2}}, \tag{8}$$

where ϵ_0 is the permittivity of free space, k_B is Boltzmann's constant, T_e is the electron temperature, n_e is the electron density, and q_e is the elementary charge. The "worst case" GEO environment has an electron density of 3e6 m^{-3} and temperature of 12E3 eV, or a Debye length of approximately 470 meters. The plasmasheet, which may be considered a GEO-like cislunar environment, has an average electron density of 2.2e5 m^{-3} and temperature of 150eV, or a Debye length of approximately 194 meters [40]. The maximum separation distance investigated in this problem is 60 meters, thus the Debye shielding is considered a secondary effect.

The gyroradius, or the radius of the circular motion of a non-relativistic charged particle in a magnetic field, is

$$r_g = \frac{v_\perp m_e}{q_e B} \tag{9}$$

where $v_\perp$ is the velocity perpendicular to the magnetic field, m_e is the mass of an electron in kilograms, and B is the magnetic field strength in Teslas. The thermal velocity of an electron is

$$v_e = \sqrt{\frac{2 k_B T_e}{m_e}}. \tag{10}$$

The geomagnetic field in GEO orbit is 100 nT, resulting in gyroradii of 100–3000 m for electron energies from 10 to 10^4 eV assuming the electron velocity is entirely perpendicular to the magnetic field [2]. The field in the plasmasheet may be on the order of 20 nT [41], resulting in gyroradii of 355-11000 m for for electron energies from 10 to 10^4 eV. This is again larger than the maximum separation distance and is considered a secondary effect.

The distance at which particles travel between collisions is characterized by the mean free path, λ_{mfp}. The mean free path of particles in a Maxwellian plasma is [42]

$$\lambda_{\text{mfp}} = \frac{48\sqrt{6/\pi} N_D \lambda_D}{\ln(9 N_D)}, \tag{11}$$

where N_D is the Debye number, or the number of particles in a sphere with radius equal to the Debye length

$$N_D = \frac{4}{3}\pi n_e \lambda_D^3. \tag{12}$$

The mean free path in GEO is approximately 3.5e5 km for worst case GEO data, and is approximately 2.7E9 km for mean plasma sheet characteristics [40]. Therefore, assuming a collisionless, vacuum model is appropriate in these environments, and the models utilized are valid.

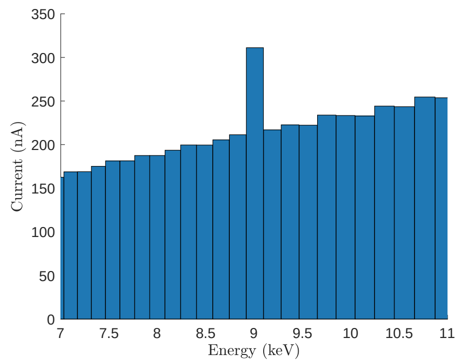

Fig. 4 Model of RPA signal for secondary electron current of 100 nA from a -13keV servicer to a -4keV target. Measurements are binned for an RPA with an energy resolution of 2%

Table 1 Electron beam variable parameters

Beam parameter	Range
Beam Energy (E_B)	1 to 30 keV
Beam Current (I_B)	10 nA to 100 μA
Deflection Angle (γ)	-2° to 2°
Half Angle (α)	0.2° to 2°

The electron flux from the ambient environment must also be considered, as the secondary electron flux must be distinguishable from the environment. The distribution of ambient electron current density to a charged spherical spacecraft as a function of velocity distribution in a Maxwellian plasma is [20, 28]

$$J(E_2) - J(E_1) = \frac{q_e n_e (1 + q_e V_s / k_B T_e)}{(2\pi m_e)^{1/2} (k_B T_e)^{3/2}} \int_{E_1}^{E_2} e^{-E/k_B T_e} E \mathrm{d}E \quad \text{for V} \geq 0, \tag{13a}$$

$$J(E_2) - J(E_1) = \frac{q_e n_e e^{V_s / k_B T_e}}{(2\pi m_e)^{1/2} (k_B T_e)^{3/2}} \int_{E_1}^{E_2} e^{-E/k_B T_e} E \mathrm{d}E \quad \text{for V} < 0. \tag{13b}$$

where V_s is the servicer potential and E is the electron energy, or $E = \frac{1}{2} m_e v_e^2$ assuming non-relativistic particles. For the spacecraft potentials, collection area, and RPA resolution defined in Sections IV, IV.B, and III, respectively, the maximum current measured by the RPA in the worst case GEO environment is approximately 360 nA. As a conservative estimate, it is assumed that the measured emissions should be on the same order of magnitude as the ambient environment, or 100 nA. As shown in Fig. 4, the RPA measurement bin containing the secondary electron emissions is distinguishable from the ambient environment and may be utilized to determine the target potential. The ambient x-ray noise is considered to be negligible for this work.

V. Electron Beam Control

The impact of beam parameters on detected emissions is first investigated to identify the most significant parameters, and those that should be prioritized when attempting to find source regions, or regions in which emissions are detectable. The range of possible beam parameters is shown in Table 1. The results are then used to determine an efficient beam control.

A. Sensing Secondary Electrons

The detected secondary electron current for a separation distance of 20 meters with the two spacecraft directly parallel to one another and a beam current of 10μA is shown in Fig. 5. As mentioned previously, the secondary electron trajectories are dependent on the geometry of the target. The target's solar panel is in the positive y-direction, or in the

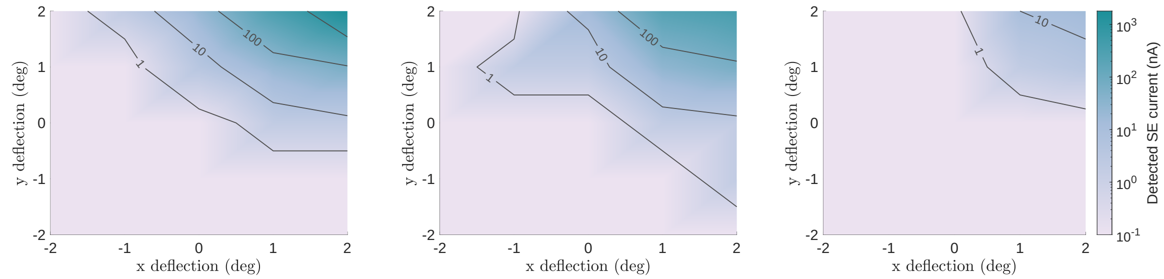

(a) E_B=10 keV, E_{land}=1 keV, half angle=0.2° (b) E_B=14 keV, E_{land}=5 keV, half angle=0.2° (c) E_B=18 keV, E_{land}=9 keV, half angle=0.2°

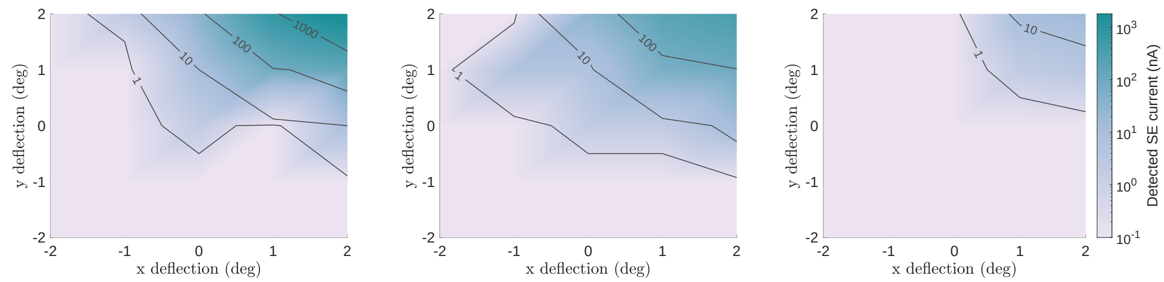

(d) E_B=10 keV, E_{land}=1 keV, half angle=1° (e) E_B=14 keV, E_{land}=5 keV, half angle=1° (f) E_B=18 keV, E_{land}=9 keV, half angle=1°

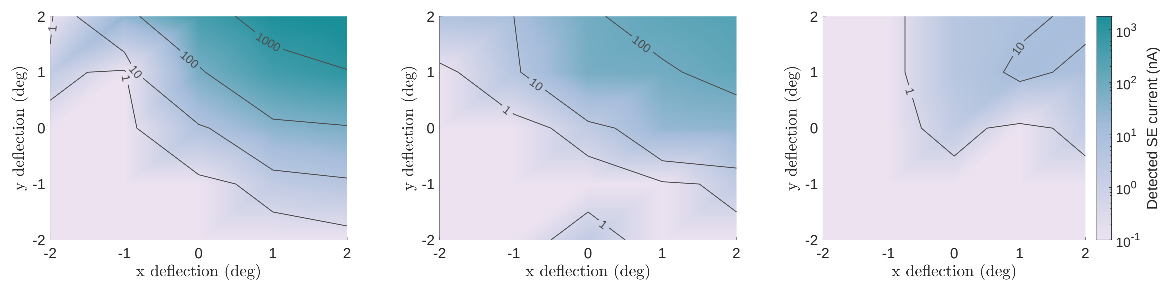

(g) E_B=10 keV, E_{land}=1 keV, half angle=2° (h) E_B=14 keV, E_{land}=5 keV, half angle=2° (i) E_B=18 keV, E_{land}=9 keV, half angle=2°

Fig. 5 Detected secondary electron current in nA for a separation distance of 20 meters and beam current of 10 μA

direction of the positive y-deflections shown in the graph. The target's boom is in the positive x-direction, or in the direction of the positive x-deflections shown in the graph. The region in which emissions are detected is in the top right corner of the plots, or when the beam is directed towards both the solar panel and the boom. This occurs because the solar panel and boom components deflect the beam and secondary emissions in the negative x and y directions according to the presented plots. The impact position of the beam must be deflected to account for this. In other words, the source region for this example is located in the top right corner of the plots, as indicated by the dark blue contours.

Increasing the half angle of the beam increases the likelihood that some or all of the beam will reach a source region, as the area of detectable emissions increases with increasing half angles in Fig. 5. Furthermore, a lower beam energy generates a higher magnitude of secondary electron current and a larger source region. Lower beam energies result in higher secondary electron yields and larger uncertainty in the landing area on the target. Since lower beam energies result in a larger source region, it may be interpreted that the magnitude of emissions is more important than the uncertainty in the beam impact position. Therefore, the electron beam energy should be minimized when possible. Overall, it appears that deflecting the beam in the direction of asymmetric components, minimizing the beam energy, and maximizing the half angle of the beam increases the likelihood that the beam will impact a source region.

From these results, the beam control is designed such that the time it takes to find the source region is minimized. To do so, at a specified beam deflection, the other parameters are swept through the possible ranges to eliminate that target impact point before changing the deflection and attempting again. The half angle is kept at the maximum of 2° to increase the probability of impacting a source region. The current is swept through 10 and 100 μA to minimize the impact of the electron beam on the potential of the target. The initial beam energy is determined such that the landing energy is 1 keV based on the initial guess of the target's potential

$$E_B, 0 = V_{T,guess} - V_S + 1E3eV. \tag{14}$$

If there is no prior knowledge of the target's potential, the initial assumption is that the target potential is equal to the servicer's potential. Otherwise, the target's potential is assumed to be equal to the potential at the time of the previous measurement. From the initial guess, the beam energy is increased in step sizes of 4 keV until it reaches the maximum energy of 30 keV. This step size is selected because the secondary electron current is sufficient at energies of 10 keV and 14 keV in Fig. 5, or 4 keVs apart. Therefore, stepsizes of 4 keV should result in one or two beam energies in which sufficient secondary electron current is excited.

The initial deflection angle is set equivalent to the deflection from the previous run, as the servicer's attitude is constrained such that it points towards the target's docking system. As a result, equivalent deflections may impact approximately the same position on the target for varying relative positions. If there is no previous measurement, the initial measurement is conducted with no deflection. If the emissions are not sufficient, the deflection angles are changed such that the distance from the initial guess increases until the entire deflection space has been investigated or the current measured is sufficient to determine the target's potential. An example of this for an initial zero deflection is demonstrated in Fig. 6. The red dots represent impact points on the target's surface, the arrows shows the order in which the points are investigated. The deflection path is shown on top of the detected secondary electron contour for a beam energy of 10 keV and half angle of 2° from Fig. 5. For this example, a sufficient current of at least 100 nA is measured on the second point, thus the control would end there.

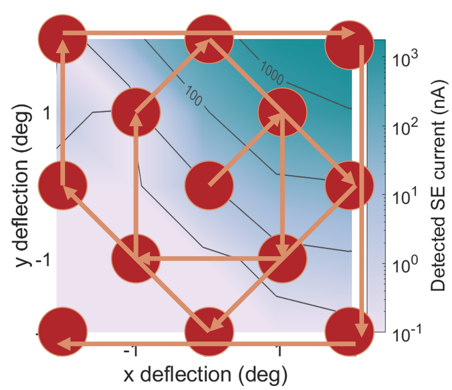

Fig. 6 Schematic of the path the beam impact points (red) follow from an initial position with no deflection. The path is shown on the sensed secondary electron current results for a beam energy of 10 keV and half angle of 2°. In this example, the second, sixth, seventh, and eleventh points impact a region in which a current of at least 100 nA is sensed.

B. Sensing X-rays

The detected x-rays for a separation distance of 20 meters with the two spacecraft directly parallel to one another and a beam current of 10μA is shown in Fig. 7. There is little variation in the detected photons as the deflection angle of the beam changes, as the beam is impacting the target for the entire range shown. The half angle also appears to have negligible impact on the detected emissions. Most notably, the magnitude of photon emissions increases as the energy of the beam increases.

The electron beam energy should be maximized, and the beam should hit the target in order for photons to be detected. Therefore, the beam energy is held at the maximum of 30 keV, and the half angle is set at the maximum of 2° to maximize the probability that the beam will impact the target. The initial attempt will be at a zero deflection, but should this not be sufficient the beam will deflect in the manner described in Section V.A. The current will be swept through 1, 10, and 100μA to minimize the change in potential imparted on the target while using the high energy electron beam. Other methods such as pulsing the beam may be utilized to minimize charging the target [43]. The x-ray

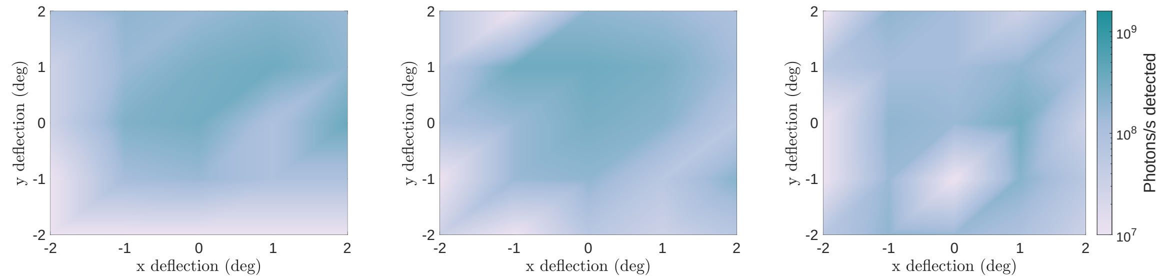

(a) E_B=20 keV, E_{land}=11 keV, half angle=0.2° (b) E_B=20 keV, E_{land}=11 keV, half angle=1° (c) E_B=20 keV, E_{land}=11 keV, half angle=2°

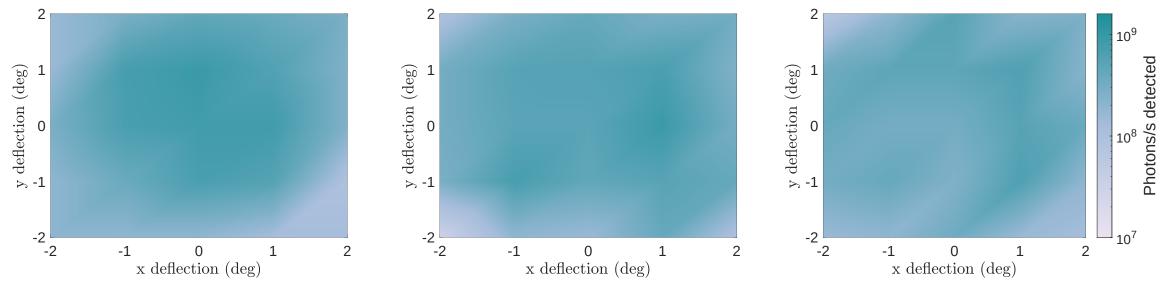

(d) E_B=30 keV, E_{land}=21 keV, half angle=0.2° (e) E_B=30 keV, E_{land}=21 keV, half angle=1° (f) E_B=30 keV, E_{land}=21 keV, half angle=0.2°

Fig. 7 Detected photons per second for a separation distance of 40 meters and beam current of 10 μA

sensor will attempt to detect a current for 100 seconds, and if sufficient photons are not detected within this time the beam parameters will be altered.

VI. Sensing Integration with Docking Problem

The developed beam controls are tested at the hold points defined in the approach trajectory in [7]. An overview of the approach trajectory is presented, and the success of the beam controls during the trajectory is evaluated.

A. Docking Problem Overview

The dynamics presented in [7] are implemented in this work. The control is implemented for two spacecraft in GEO orbit subject to perturbations due to solar radiation pressure (SRP) and electrostatic forces and torques. The electrostatic perturbations are computed using the multi-sphere model (MSM). The multi-sphere model (MSM) discretizes a spacecraft model into spheres for rapid computation of electrostatic interactions with a fraction of computational cost compared to finite element formulation [7, 44]. The charge Q_i on the discretized spheres may be computed using the mutual and self capacitance of the spheres for a given voltage V_i, radius R_i, and separation distance $r_{i,j}$ as

$$\begin{bmatrix} V_1 \\ V_2 \\ \vdots \\ V_3 \end{bmatrix} = k_c \begin{bmatrix} 1/R_1 & 1/r_{1,2} & \dots & 1/r_{1,n} \\ 1/r_{2,1} & 1/R_2 & \dots & 1/r_{2,n} \\ \vdots & \vdots & \ddots & \vdots \\ 1/r_{n,1} & 1/r_{n,2} & \dots & 1/R_n \end{bmatrix} \begin{bmatrix} q_1 \\ q_2 \\ \vdots \\ q_n \end{bmatrix}, \tag{15}$$

where k_c is Coulomb's constant ($\approx$ 8.99E9 Nm^2/C^2). Once the charges are determined, the force **F** and torque **L** on body 2 due to body 1 is

$$\mathbf{F} = k_c \sum_{j=1}^{n_1} q_j \left(\sum_{i=1}^{n_2} \frac{q_i}{r_{i,j}^3} \mathbf{r_{i,j}} \right), \tag{16}$$

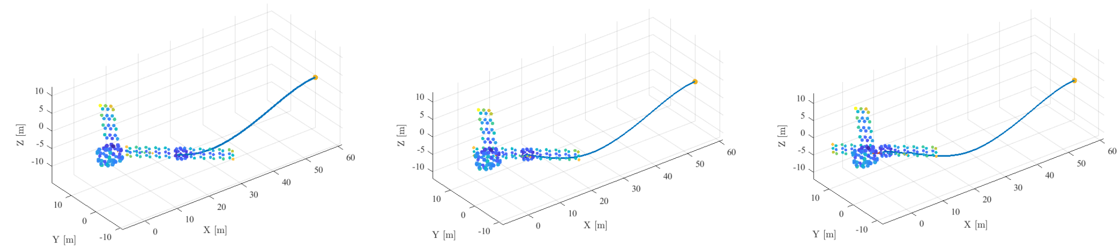

(a) 20 m separation (b) 10 m separation (c) 3 m separation

Fig. 8 Spacecraft positions and trajectories at the hold points

$$\mathbf{L} = k_c \sum_{j=1}^{n_1} q_j \left(\sum_{i=1}^{n_2} \frac{q_i}{r_{i,j}^3} \mathbf{r_i} \times \mathbf{r_{i,j}} \right), \tag{17}$$

where $\mathbf{r_i}$ is the distance from the center of the sphere to the center of mass of the body. The simulation is performed with 80 spheres for the target and 92 for the servicer. For comparison, a higher-fidelity model, composed of four times more spheres requires a six times higher computation time with little changes in results [7].

Utilizing the multi-sphere model, an optimized predictor-corrector control is presented that minimizes the final rotational velocity of the target. Position and attitude constraints require the target to be within a 25° cone of the docking port of the target, and the servicer is pointed towards the docking point on the target. This leaves only the roll angle of the servicer free in the target Hill frame and keeps the servicer within the line of sight of the docking port. The approach trajectory is set to initialize at 60 m, and hold points are defined at 20, 10, and 3 meters of separation for 10 minutes each, and the trajectories and position's at these hold points are shown in Fig. 8. This control has a significant computation time, and thus most likely must be implemented on the ground or during hold times. Therefore, the potential measurements and trajectory updates are defined to occur at the hold times.

For this work, the servicer and target start with potentials of -4 kV and -13 kV, respectively, based on NASCAP-2k potential estimates of the Orion and Lunar Gateway during docking operations in GEO [45]. The spacecraft linearly approach an equivalent potential of -8.5 kV over the course of the docking problem. This represents a scenario in which the difference in potentials is mitigated before the spacecraft dock and allows for insight into the impact of varying potentials on potential sensing.

B. Sensing with Secondary Electron

The final beam parameters and time it takes to determine the target's potential is shown in Table 2. The excited secondary electron emissions are detectable at all the tested relative positions, and as the separation distance decreases, the beam current required to excite sufficient secondary electron current decreases. The time to determine the target potential at the initial position is approximately 4 minutes. The beam does not have to be deflected to excite detectable secondaries, but the target's potential is initially assumed to be equal to the servicer's potential, for an error 9 keV more positive. Thus, finding the ideal beam energy requires an extended period of time. At 20 meters of separation, it takes approximately 20 minutes to determine the target's potential, about twice as long as the ideal hold time. This occurs

Table 2 Final beam parameters and sensing times using secondary electron emissions

Separation Distance	Servicer Potential (eV)	Target Potential (eV)	Final Beam Energy (eV)	Final Beam Current (μA)	Final Defl. (x°,y°)	Total Time
60	-4000	-13000	13000	100	(0,0)	234 s / 3.9 min
20	-5355	-11645	8645	100	(1,-1)	1208 s / 20.1 min
10	-6994	-10006	5651	10	(1,-1)	25 s
3	-7985	-90149	3021	10	(1,-1)	22 s

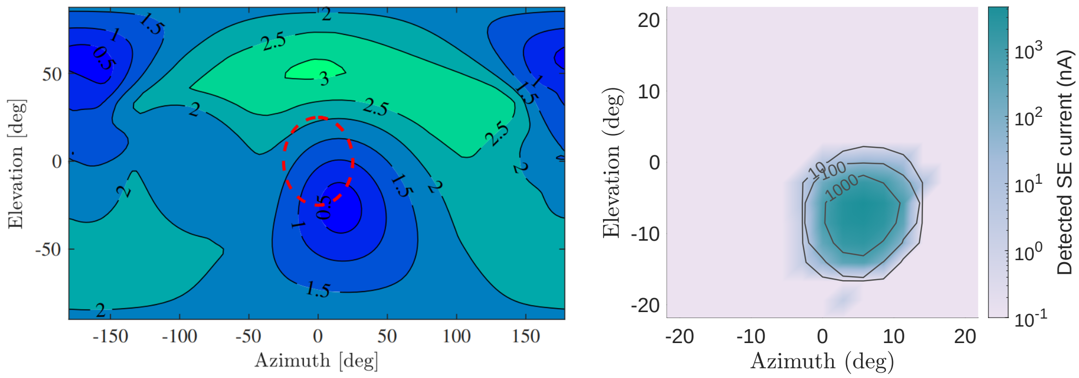

(a) Electrostatic torques acting on GOES-R at a 10 m distance. The circled region corresponds to a 25° approach cone [7].

(b) Detected secondary electron current for varying servicer positions at a separation distance of 20 m

Fig. 9 Electrostatic torques and detected secondary electron current in nA for varying servicer positions with respect to the target.

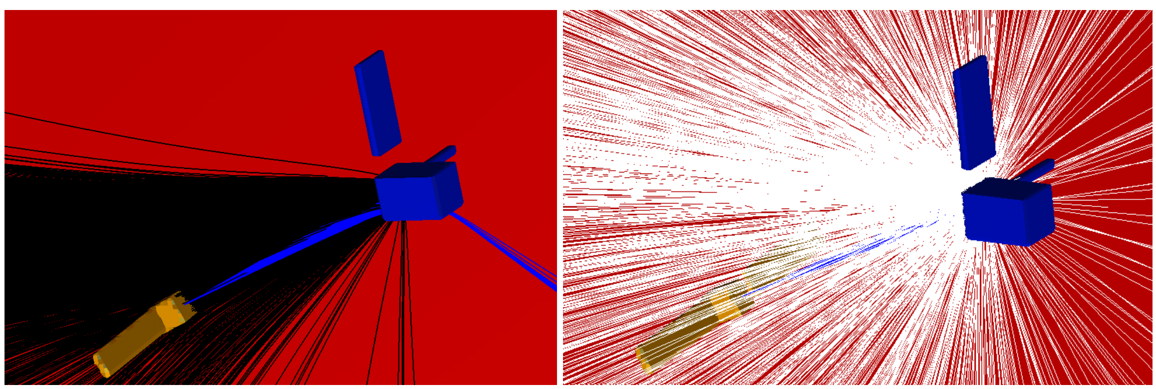

(a) Secondary electron emissions

(b) Photoelectron emissions

Fig. 10 Electron beam (blue) and emission trajectories for a -5355 V servicer (orange) and -11645 V target (blue) at a separation distance of 20 m.

because the initial beam deflection is not within the source region and is varied until the final deflection point is found (Fig. 10). However, the final beam deflection found at the 20 m hold point works for the following hold points, and as a result both only take 20 to 30 seconds to determine the target's potential. This validates that utilizing the beam deflection from a previous measurements provides an efficient means of finding secondary electron source regions.

It is interesting that secondary electron emissions are available at all the tested relative positions, as secondary emissions are typically only detectable for a fraction of relative positions when the beam parameters are held constant [15, 19]. This may indicate that manipulating the beam parameters increases the fraction of regions in which secondaries may be detected. To further investigate why these positions are feasible for secondary electron detection, the position of the servicer at -4 keV with respect to the target at -13 keV is varied for 20 m of separation, a 10keV beam, half angle of 2°, and no beam deflection. Upon comparing this to the electrostatic torques determined in [7], it is found that the region in which the torques are smallest roughly correlates to the region in which the secondary electron emissions are detected, as shown in Fig. 9. Therefore, adjusting the servicer position such that electrostatic torque on the target is minimized may improve the probability that secondary electron emissions are detectable.

Table 3 Final beam parameters and sensing times using x-ray emissions

Separation Distance	Servicer Potential (eV)	Target Potential (eV)	Final Beam Current (μA)	Final Defl. (x°,y°)	Total Time
60	-4000	-13000	1	(0,0)	55 s
20	-5355	-11645	1	(1,1)	383 s / 6.4 mins
10	-6994	-10006	1	(0,0)	15 s
3	-7985	-90149	1	(0,0)	1 s

C. Sensing with X-rays

The x-ray control is simpler and faster than the secondary electron control, as expected, as shown in Table 3. In addition, the beam current required to produce sufficient photons is 1 μA, smaller than that required for secondary electrons. Once again, the deflection of the beam is altered at a 20 m of separation (Fig. 10, increasing the detection time from seconds to minutes. However, the detection time remains smaller than the hold time of 10 minutes. These results follow the expected trends, and x-ray emissions may be utilized for touchless potential sensing scenarios where speed is desired over accuracy.

D. Fusion of Methods

As previously mentioned, touchless potential sensing is less accurate when utilizing x-rays. However, as shown, exciting and detecting x-ray emissions is simpler and faster than secondary electrons. Therefore, it is desirable to fuse the two sensing methods such that x-rays are first detected and the targets potential is determined within approximately $\pm$120 V. Once an approximation of the target's potential is determined, the beam energy is then selected such that the landing energy is $\approx$1 keV. The beam is then swept through the deflection points defined in Section V until sufficient secondaries are detected.

It should be noted that the beam current utilized to determine x-rays is set to a constant 1μA instead of sweeping through 1, 10, and 100μA as previously defined. This change is implemented becaused results in Table 3 show that a beam current of 1μA is sufficient at all separation distances. The results of the fused control are shown in Table 4. The sensing time is faster or within a few seconds of the sensing times when detecting only secondary electron emissions in Table 2. This occurs because the beam energy is held constant at the near optimal energy for secondary electron emissions and only the beam current is varied at each deflection angle. Furthermore, in Section V it is shown that the source region is larger at a landing energy of 1 keV than higher beam energies. So, there are more deflection angles at which secondary electron emissions may be detected. Overall, as desired, fusing the two sensing methods allows secondary electron source regions to be found more efficiently.

VII. Conclusion

The effect that manipulating beam properties has on the ability of a servicing craft to employ remote potential sensing techniques is investigated. It is found that the energy of the beam and deflection angle have the largest impact on the magnitude of secondary electrons detected. X-ray emissions are maximized for larger beam energies and experience little change when other beam parameters, such as half angle or deflection angle, vary.

The proposed manner in which the electron beam properties should be changed is tested in a scenario in which a

Table 4 Final beam parameters and sensing times using x-ray and secondary electron emissions

Separation Distance	Servicer Potential (eV)	Target Potential (eV)	Final Beam Energy (eV)	Final Beam Current (μA)	Final X-ray / SE Deflections (x°,y°)	Total Time
60	-4000	-13000	10000	100	(0,0) / (0,0)	112 s / 1.8 min
20	-5355	-11645	7300	100	(1,1) / (1,-1)	333 s / 5.6 min
10	-6994	-10006	4100	100	(0,0) / (1,-1)	37 s
3	-7985	-90149	2200	10	(0,0) / (1,-1)	22 s

servicer approaches a target, and the potentials of both craft vary. It takes several minutes to determine the correct beam energy and deflections when searching for secondary electron emissions. However, once the optimal deflection and beam energy are determined, future efforts to detect secondary electron emissions may be conducted in less than a minute, regardless of changing spacecraft potentials. X-ray emissions are more easily found, as expected, and detecting these emissions takes a few seconds to a couple minutes. Fusing the two methods allows for secondary electron emissions to be determined more efficiently than sensing using secondary electrons alone. This may allow fora target's potential to be determined without sacrificing speed or accuracy. Future work may involve utilizing photoelectron emissions in addition to x-ray or secondary emissions, as this may decrease the sensing time and allow for active control of the target's potential to be implemented.

It is also found that secondary electron and x-ray emissions are available at all tested relative positions. This is encouraging, as secondary electrons have previously been available for approximately 10% of relative positions when the beam parameters are held constant [18]. Thus, altering the beam parameters may allow for secondaries to be detected at more relative positions than previously expected. Investigations also show that the region in which secondaries are detected for a beam with no deflection roughly aligns with low electrostatic torque regions found in [7]. Therefore, adjusting the servicer position such that electrostatic torque on the target is minimized may improve the probability that secondary electron emissions are detectable. Future work will investigate this relationship.

Acknowledgments

This work was supported by a NASA Space Technology Graduate Research Opportunity.

References

[1] Bengtson, M. T., Wilson, K. T., and Schaub, H., "Experimental Results of Electron Method for Remote Spacecraft Charge Sensing," *Space Weather*, Vol. 18, No. 3, 2020, pp. 1–12. https://doi.org/10.1029/2019SW002341.

[2] 'Alvaro Romero Calvo, Hammerl, J., and Schaub, H., "Touchless Potential Sensing of Complex Differentially-Charged Shapes Using Secondary Electrons," *AIAA Journal of Spacecraft and Rockets*, Vol. 59, No. 5, 2022, pp. 1623–1633. https://doi.org/10.2514/1.A35355.

[3] Wilson, K. T. H., and Schaub, H., "X-Ray Spectroscopy for Electrostatic Potential and Material Determination of Space Objects," *IEEE Transactions on Plasma Science*, Vol. 47, No. 8, 2019, pp. 3858–3866. https://doi.org/10.1109/TPS.2019.2910576.

[4] Wilson, K. T., Bengtson, M. T., and Schaub, H., "X-ray Spectroscopic Determination of Electrostatic Potential and Material Composition for Spacecraft: Experimental Results," *Space Weather*, Vol. 18, No. 4, 2020, p. e2019SW002342. https://doi.org/10.1029/2019SW002342.

[5] Álvaro Romero Calvo, Champion, K., and Schaub, H., "Touchless spacecraft potential sensing using energetic electron beams and active photoemission," *Proceedings of the Spacecraft Charging and Technologies Conference*, 2022.

[6] Wilson, K., and Schaub, H., "Impact of Electrostatic Perturbations on Proximity Operations in High Earth Orbits," *Journal of Spacecraft and Rockets*, Vol. 58, No. 5, 2021, pp. 1293–1302. https://doi.org/10.2514/1.A35039.

[7] Wilson, K., Romero-Calvo, A., and Schaub, H., "Constrained Guidance for Spacecraft Proximity Operations Under Electrostatic Perturbations," *Journal of Spacecraft and Rockets*, Vol. 0, No. 0, 2022, pp. 1–13. https://doi.org/10.2514/1.A35162, *in press*.

[8] Schaub, H., Parker, G. G., and King, L. B., "Challenges and Prospects of Coulomb Spacecraft Formation Control," *The Journal of the Astronautical Sciences*, Vol. 52, No. 1, 2004, pp. 169–193. https://doi.org/10.1007/BF03546427.

[9] Casale, F., Schaub, H., and Biggs, J. D., "Lyapunov Optimal Touchless Electrostatic Detumbling of Geostationary Debris Using Surface Multisphere Models," *AIAA Journal of Spacecraft and Rockets*, Vol. 58, No. 3, 2021. https://doi.org/10.2514/1.A34787.

[10] Schaub, H., and Moorer, D. F., "Geosynchronous Large Debris Reorbiter: Challenges and Prospects," *The Journal of the Astronautical Sciences*, Vol. 59, No. 1, 2012, pp. 161–176. https://doi.org/10.1007/s40295-013-0011-8.

[11] Hughes, J., and Schaub, H., "Prospects of Using a Pulsed Electrostatic Tractor With Nominal Geosynchronous Conditions," *IEEE Transactions on Plasma Science*, Vol. 45, No. 8, 2017, pp. 1887–1897.

[12] Bengtson, M., Wilson, K., Hughes, J., and Schaub, H., "Survey of the electrostatic tractor research for reorbiting passive GEO space objects," *Astrodynamics*, Vol. 2, No. 4, 2018, pp. 291–305.

[13] Hughes, J. A., and Schaub, H., "Electrostatic Tractor Analysis Using a Measured Flux Model," *Journal of Spacecraft and Rockets*, Vol. 57, No. 2, 2020, pp. 207–216.

[14] Hammerl, J., and Schaub, H., "Effects of Electric Potential Uncertainty on Electrostatic Tractor Relative Motion Control Equilibria," *Journal of Spacecraft and Rockets*, Vol. 59, No. 2, 2022, pp. 552–562. https://doi.org/10.2514/1.A35165.

[15] Bengtson, M., Hughes, J., and Schaub, H., "Prospects and Challenges for Touchless Sensing of Spacecraft Electrostatic Potential Using Electrons," *IEEE Transactions on Plasma Science*, Vol. 47, No. 8, 2019, pp. 3673–3681.

[16] Bengtson, M. T., and Schaub, H., "Electron-Based Touchless Potential Sensing of Shape Primitives and Differentially-Charged Spacecraft," *Journal of Spacecraft and Rockets*, Vol. 58, No. 6, 2021, pp. 1847–1857. https://doi.org/10.2514/1.A35086.

[17] 'Alvaro Romero Calvo, Hammerl, J., and Schaub, H., "Touchless Potential Sensing of Complex Differentially-Charged Shapes Using Secondary Electrons," *AIAA Journal of Spacecraft and Rockets*, Vol. 59, No. 5, 2022, pp. 1623–1633. https://doi.org/10.2514/1.A35355.

[18] Wilson, K., Bengtson, M., and Schaub, H., "Remote Electrostatic Potential Sensing for Proximity Operations: Comparison and Fusion of Methods," *Journal of Spacecraft and Rockets*, 2022. *under review*.

[19] Wilson, K., and Schaub, H., "Predictive Control For Spacecraft Proximity Operations Under Electrostatic Perturbations," *Proceedings of the IEEE Aerospace Engineering Conference, Big Sky, Montana*, 2021.

[20] Lai, S. T., *Fundamentals of Spacecraft Charging: Spacecraft Interactions with Space Plasmas*, Princeton University Press, 2012.

[21] Garrett, H. B., and Whittlesey, A. C., "Spacecraft Design Guidelines," *Guide to Mitigating Spacecraft Charging Effects*, John Wiley & Sons, Ltd, 2012, Chap. 3, pp. 26–61. https://doi.org/10.1002/9781118241400.ch3.

[22] Cho, M., Kawakita, S., Nakamura, M., Takahashi, M., Sato, T., and Nozaki, Y., "Number of arcs estimated on solar array of a geostationary satellite," *Journal of spacecraft and rockets*, Vol. 42, No. 4, 2005, pp. 740–748.

[23] Roe, R., *Mitigating In-Space Charging Effects-A Guideline*, National Aeronautics and Space Administration, 2022. URL https://standards.nasa.gov/sites/default/files/standards/NASA/B/0/2022-06-07-NASA-HDBK-4002B-Approved.pdf.

[24] Bengtson, M. T., "Electron Method for Touchless Electrostatic Potential Sensing of Neighboring Spacecraft," Ph.D. thesis, University of Colorado Boulder, 2020. URL http://hanspeterschaub.info/Papers/grads/MilesBengtson.pdf.

[25] Sanders, N. L., and Inouye, G. T., "Secondary emission effects on spacecraft charging: Energy distribution considerations," *Spacecraft Charging Technology*, 1978, pp. 747–755. NASA-2071, ADA-084626.

[26] Chung, M. S., and Everhart, T. E., "Simple calculation of energy distribution of low-energy secondary electrons emitted from metals under electron bombardment," *Journal of Applied Physics*, Vol. 45, No. 2, 1974, pp. 707–709. https://doi.org/10.1063/1.1663306.

[27] Bruining, H., *Physics and Applications of Secondary Electron Emission*, New York: McGraw-Hill Book Co., Inc. London: Pergamon Press Ltd., 1954. Chapter 7: Theory of Secondary Electron Emission; Discussion of Some Properties of Secondary Electrons.

[28] Lai, S. T., and Miller, C., "Retarding potential analyzer: Principles, designs, and space applications," *AIP Advances*, Vol. 10, No. 9, 2020, p. 095324. https://doi.org/10.1063/5.0014266.

[29] Case, A. W., Kasper, J. C., Stevens, M. L., Korreck, K. E., Paulson, K., Daigneau, P., Caldwell, D., Freeman, M., Henry, T., Klingensmith, B., et al., "The solar probe cup on the Parker Solar Probe," *The Astrophysical Journal Supplement Series*, Vol. 246, No. 2, 2020, p. 43.

[30] Fanelli, L., Noel, S., Earle, G., Fish, C., Davidson, R., Robertson, R., Marquis, P., Garg, V., Somasundaram, N., Kordella, L., et al., "A versatile retarding potential analyzer for nano-satellite platforms," *Review of Scientific Instruments*, Vol. 86, No. 12, 2015.

[31] Wilson, K., Álvaro Romero-Calvo, Bengtson, M., Hammerl, J., Maxwell, J., and Schaub, H., "Development and characterization of the ECLIPS space environments simulation facility," *Acta Astronautica*, Vol. 194, 2022, pp. 48–58. https://doi.org/https://doi.org/10.1016/j.actaastro.2021.12.037.

[32] Enloe, C., "High-resolution retarding potential analyzer," *Review of scientific instruments*, Vol. 65, No. 2, 1994, pp. 507–508.

[33] Wilson, K. T., “Remote Electrostatic Potential Determination for Spacecraft Relative Motion Control,” Ph.D. thesis, Aerospace Engineering Sciences Department, University of Colorado, Boulder, CO, 2021.

[34] Van Grieken, R. E., and Markowicz, A. A., *Handbook of X-Ray Spectrometry*, Marcel Dekker Inc., 2001. Second Edition.

[35] McCall, G. H., “Calculation of X-ray bremsstrahlung and characteristic line emission produced by a Maxwellian electron distribution,” *Journal of Physics D: Applied Physics*, Vol. 15, No. 5, 1982, p. 823.

[36] Wilson, K. T. H., Hammerl, J., and Schaub, H., “Using Plasma-Induced X-Ray Emission to Estimate Electrostatic Potentials on Nearby Space Objects,” *Journal of Spacecraft and Rockets*, Vol. 59, No. 4, 2022, pp. 1402–1405. https://doi.org/10.2514/1.A35161.

[37] Champion, K. M., Romero-Calvo, Á., and Schaub, H., “Large scale particle tracing simulation for touchless potential sensing,” *AIAA SCITECH 2023 Forum*, 2023, p. 1770.

[38] Romero Calvo, A., Champion, K., and Schaub, H., “Enabling Ultraviolet Lasers for Touchless Spacecraft Potential Sensing,” *IEEE Transactions on Plasma Science*, Vol. 51, No. 9, 2023, pp. 2468–2481. https://doi.org/10.1109/TPS.2023.3264914.

[39] Fahr, Hans J., and Heyl, M., “Debye screening under non-equilibrium plasma conditions,” *Astronomy & Astrophysics*, Vol. 589, 2016, p. A85. https://doi.org/10.1051/0004-6361/201628082.

[40] Leahy, F. B., “SLS-SPEC-159, Cross-Program Design Specification for Natural Environments (DSNE),” Tech. rep., National Aeronautics and Space Administration, 2021.

[41] Meng, C.-I., and Mihalov, J., “Average plasma-sheet configuration near 60 earth radii,” *Journal of Geophysical Research*, Vol. 77, No. 10, 1972, pp. 1739–1755.

[42] Livadiotis, G., “Collision frequency and mean free path for plasmas described by kappa distributions,” *AIP Advances*, Vol. 9, No. 10, 2019, p. 105307. https://doi.org/10.1063/1.5125714, URL https://doi.org/10.1063/1.5125714.

[43] Walker, J., Hammerl, J., and Schaub, H., “Experimental Concept Validation of Touchless Electric Potential Sensing using a Pulsed Electron Beam,” *AIAA SciTech*, National Harbor, Maryland, 2023.

[44] Stevenson, D., and Schaub, H., “Multi-Sphere Method for modeling spacecraft electrostatic forces and torques,” *Advances in Space Research*, Vol. 51, No. 1, 2013, pp. 10 – 20.

[45] McCollum, M., Willis, E., and Diekmann, A., “Artemis IV Docking in Radiation Belt Charging Environment,” , Aug. 2023. URL https://spaceweathersolutions.com/proceedings/.